Clog and Crack: Opening and Closing Behavior During a Sustained Explosive Eruption as recorded by its Hidden Earthquakes

Ricardo Garza-Giron[1], Emily E. Brodsky[1], Zack J. Spica[2] and Matthew M. Haney[3]

1. Department of Earth and Planetary Sciences, University of California, Santa Cruz, Santa Cruz, CA 95060, USA.

2. Department of Earth and Environmental Sciences, University of Michigan, Ann Arbor, MI 48109, USA.

3. Alaska Volcano Observatory, USGS Alaska Science Center, Anchorage, AK, 99508, USA.

Abstract

Volcanic eruptions progress by co-evolving fluid and solid systems. The fluid mechanics can be observed through the plumes and ejecta produced, but how does the solid system evolve? When does the conduit open? When does it close? Seismology can potentially tell us about these processes by measuring the failure of the solid rock. Such inferences require the detection of earthquakes during an explosive eruption. Standard earthquake detection methods often fail during this time as the eruption itself produces seismic waves that obscures the earthquake signals. We address this problem by applying supervised and unsupervised search techniques to the existing catalog of the 2008 Okmok eruption to find brittle failure signals during the continuous eruptive sequence. The interaction between fluid pathways and seismicity is reinforced by high precision earthquake relocations that highlight a ring-fault structure, which may be acting as a conduit for fluids to the surface. The timing of the earthquakes during the eruption reveal that the seismicity gradually increases during the vent-opening stage

(July 12-July 24), peaks during the vent-widening stage (July 24-August 1) which culminates in a large burst of earthquakes, and then gradually decrease until the end of the eruptive period. Seismic bursts during the eruption are not synchronized with the exhalation of large ash and steam plumes. In other words, when the system is closed, the rock breaks. We call this scenario clog and crack.

Plain Language Summary

We studied the occurrence of earthquakes during a long-lived eruption by using modern techniques to find events that would otherwise remain hidden in the complex, continuous seismic record. We increased the number of observed events by almost one order of magnitude and we calculated the magnitude of all the earthquakes by calibrating a local magnitude scale for the region. This new high-resolution data set unveils a dynamic interaction between the solid medium and the fluids that we call clog and crack. When the system is closed, the rocks are stressed by the trapped pressurized fluids and then break in earthquakes. When the system is open, ash and steam plumes grow higher, the rock is not being stressed as much and the number of observed earthquakes is lower. The volcano is displaying both open and closed vent behavior through its earthquakes during a single eruption.

Keywords: Okmok volcano, earthquake detection, eruptive seismicity, eruption dynamics, caldera

Introduction

The breaking of rocks as manifested by earthquakes is an intrinsic part of volcanic eruptions. Earthquakes are the most readily observable aspect of rock failure. Seismicity is one of the most common precursors of eruptions and it often continues after an eruption ends. But what happens in between? How do the earthquakes progress during an eruption? These questions have been studied at length for effusive eruptions, but have been hampered by detection limits during sustained, large-scale explosive eruptions. Explosive eruptions produce seismic waves, as a result surviving, onscale seismograms in the near-field are usually covered with continuous waves that obscure individual earthquakes, particularly the low magnitude ones.

Recent advances in seismological processing allow a partial solution to the problem of detecting earthquakes during an explosive eruption by template matching and fingerprint similarity (Yoon et al., 2015; Shelley et al., 2016; Chamberlain et al., 2018; Wech et al., 2018). Template matching consists of using previously detected earthquakes (templates) to scan the continuous data by performing cross-correlations in order to find new events (detections). Earthquakes that occur close to one another would share a similar travel path, and thus would have a high waveform similarity, which would be reflected with a high normalized cross-correlation value. Fingerprint similarity, on the other hand, is a non-supervised method that allows us to find new events that do not have a parent template in the original catalog by matching any waveform pairs from the windowed, continuous data.

The goal of this research is to identify earthquakes in nearfield records during an extended explosive eruption for the first time. We focus on the 2008 VEI 4 eruption of Okmok Caldera as an adequately instrumented volcano where, unusually, most seismic stations survived and produced on-scale recordings for the entire 2-month sequence. By identifying these earthquakes, we will be able to produce a time series of the seismicity and place it in context of the other observations of the eruption. Resolving the full sequence of earthquakes is of particular importance for eruptions like Okmok where the vent structure appears to evolve during the eruption. As will be discussed below, earthquakes provide a window into the rock failure that otherwise is invisible to standard measurements during the eruption.

The 2008 Okmok Eruption

Okmok is a 10 km wide basaltic-andesitic caldera located on Unmak Island, in the Aleutian Arc of Alaska (Fig 1). For over a century, most of the eruptions at Okmok had their source at an intra-caldera cone (Cone A; Fig. 1 inset) and were mostly Hawaiian to Strombolian (Coats, 1950; Grey, 2003). The 2008 eruption marked a change in this behavior because of the interactions between magma and water, making new intra-caldera maar-like vents and developing a new tephra cone during a large phreato-magmatic eruption (Larsen et al., 2015).

During the 6 months preceding the eruption, the Alaska Volcano Observatory (AVO) detected only 9 low magnitude earthquakes, giving no sign of obvious precursory activity. On July 12, 2008 the seismic network at Okmok recorded the onset of a ~4.5 hour-long earthquake swarm (Johnson et al., 2010) after which explosive activity

commenced. The short sequence of precursory earthquakes has been reanalyzed by Ohlendorf et al. (2014) using the AVO catalog events, and the earthquakes originated at approximately 3 km depth beneath the intracaldera cone known as Cone D (Fig. 1 inset). The beginning of the eruption was accompanied by more than 12 hours of continuous high-amplitude seismic eruption tremor (Larsen et al., 2009). Tremor continued at variable levels throughout the 40-day-long eruption and emanated mainly from a new intracaldera cone (Haney, 2010; Haney, 2014). This new cone, to the north of Cone D and built during the 2008 eruption, was subsequently named Ahmanilix (meaning surprise in the Unangan language) Cone. After a large-scale initial plume, activity continued by opening, and perhaps widening, new vents in a westward alignment from the north-west of Cone D as well as Ahmanilix Cone. On July 19, the network recorded high-amplitude sustained tremor that lasted ~20 hours and it has been thought to be related to the temporary drainage of the long-lived North Cone D lake, which was seen by satellite imagery on July 21 (Larsen et al., 2015). Larsen et al. (2015) report that between July 24 and August 1 the North vent structure, directly to the north of Ahmanilix, widened and there was an increase in number and size of reflectors observed in SAR images, followed by an increase in ash production on August 2, confirmed by AVO staff in the field. From August 3 until August 19, when the last emision of ash was reported and the eruption officially ended, the plumes decreased in number and size.

Data and Methods

Okmok Caldera was relatively well-instrumented at the time of the eruption, although

there were some notable outages. Few large volcanic eruptions have been historically recorded with such a comparable wealth of locally recorded data. On July 12 2008, Okmok had seven short-period seismometers in addition to two broad-band stations with co-located GPS on the island. A third GPS station, OKCE, was located inside of the caldera but stopped transmitting data weeks before the eruption started and it was not restarted by AVO staff until September 11, 2008, after the eruption had ended (Freymueller and Kaufman, 2010). Besides this, some of the larger seismic events were recorded as far as Makushin and Akutan volcanoes, which had local seismic networks. With the addition of a station in the permanent Alaska Regional Network (AK) on Unalaska Island, this brings the total number of stations within 200 km of Okmok to 9 broad-band and 15 short-period instruments (Fig. 1).

We used the 419 events cataloged by AVO during the period of time July 12 -August 31, 2008 as the templates and then matched them using the waveforms in all vertical channels available. Horizontals are omitted from the analysis due to high noise and their availability on only a subset of the stations. As mentioned above, this eruption was not preceded by many earthquakes.

During large volcanic eruptions, there are many factors that depress the number of detected earthquakes in a seismic catalog. For example, there might be instrumental issues such as the loss of stations during the blasts on the volcano or outages in the data due to telemetry interference caused by the dense plumes. Similarly, there might be operational and practical challenges for the staff of the monitoring agency in charge to detect earthquakes. Earthquake waveform data is often overwhelmed by other

signals such as volcanic tremor or high noise level, impairing the efficiency of standard detection methods.

In this work, we exploit earthquake template matching tools to address at least some of these deficiencies. The cross correlation of earthquakes waveforms has proven to be a powerful tool that serves different purposes. Previous studies have made use of this tool to enhance seismic catalogs in different environments by detecting smaller earthquakes in the continuous data using the cataloged earthquakes as templates (Shelly et al., 2007; Shelly et al, 2016; Ross et al., 2019).

For template matching, we make use of the Python packages Obspy (Beyreuther et al., 2010) and EQcorrscan (Chamberlain et al., 2018) to process the data and detect events, respectively. Our procedure is fully detailed in Supplement Section 1. Potential detections are made whenever a template has an absolute cross correlation value equal or greater than 0.8 (See Example in Figure 2).

A major problem with template matching is that it can only detect new events where a previous template is available. For Okmok, this issue introduces the danger that the final catalog is biased to only include events from the subset of regions that were active at low noise times or were large enough so that the AVO catalog is able to provide good templates. To mitigate against this potential problem, we also did an unsupervised search for events using the Fingerprint And Similarity Thresholding (FAST) algorithm (Yoon et al., 2015) to extend the catalog with new detections. FAST is a highly efficient way to search for similar signals using an unsupervised approach

where every waveform of the windowed continuous data set is compared to every other window that it resembles using a locality-sensitive hashing method. The FAST procedure is also fully detailed in Supplement Section 1. We then compare results of this study against the FAST catalog to ensure robustness.

Furthermore, we used the cross-correlation information of all of the AVO catalog templates to improve the AVO event locations by using the hybrid double-difference relocation/clustering algorithm Growclust (Trugman and Shearer, 2017). The main input required by Growclust is the travel-time differences and the cross-correlation values at all stations for each pair of events. First, we assigned the P phase arrival of the newly detected events as the detection time plus 0.5s. Then, we determined the cross-correlation values of all events using 5s windows, 0.5s before the P phase and 4.5s after. The travel-time differences between events were those estimated from the phase pick files. The velocity model provided to the algorithm is a 1D layered structure model (Dixon and Stihler, 2009).

Given the average P wave velocity at Okmok ~5.7 km/s, over depths -1 to 20 km, travel time differences of <0.1s would give a relocation resolution of <560 m. Because of the sparse station coverage and limited available velocity models, we assume that the template matched events are co-located with the parent templates and in order to be able to see which region of the caldera is being activated, we simply allow their locations to be randomly distributed within 500 m of the relocated template for visualization.

As the newly added FAST events do not have a parent template to be co-located with, we located them by making P and S phase picks and using the location algorithm HYPOELLIPSE (Lahr, 1999), including the same control files that AVO used to locate the initial catalog in 2008. We then performed relocations to these earthquakes following the procedure described above (Figure S8).

The last feature that we need in order to have a complete new catalog is the magnitude of the earthquakes. A common approach to estimate the magnitude of detections is based on the ratio of the amplitudes of the detected earthquakes to the template earthquakes and the pre-determined magnitudes of the templates (Shelly et al., 2016; Wech et al., 2018). This heuristic procedure works best where the pre-existing local magnitudes are well-calibrated, which is not the case on this highly attenuating, sparsely instrumented volcano.

Therefore, we used the data to establish a local-magnitude scale based on the local attenuation relationship during the time of the eruption and for the specific operating network that we are using. We followed the procedure prescribed by Richter (1935) and the corrections noted by Hutton and Boore (1987) so that a M_L=3 earthquake has a 10mm amplitude at a 17 km hypocentral distance on a Wood-Anderson instrument:

$$M_L = log_{10}(A) - log_{10}(A_0) + dM_L \quad (1)$$

where

$$log_{10}(A_0) = \alpha\ log_{10}\left(\frac{R}{17}\right) + K\,(R - 17) - 2 \qquad (2)$$

and

A=peak-to-peak Wood-Anderson amplitude /2 (note that this is different than just the zero-to-peak amplitude)

R = Hypocentral distance in km

α = Geometric spread factor

K = Attenuation factor

dM_L=Station correction

To find the unknown parameters of these expressions, we arrange our equations so that:

$$log_{10}(A) + 2 = M_L + \alpha\ log_{10}\left(\frac{R}{17}\right) + K\,(R - 17) - dM_L \qquad (3)$$

We inverted Eq 3. to solve for M_L α, *K* and dM_L using a generalized linear least squares (Miao and Langston,2007; Menke, 2018).

We systematically process all the earthquake waveforms available, from both templates and detections, at all stations by detrending, applying a Hanning taper and a bandpass filter between 1-20 Hz and finally performing the full deconvolution of the instrument response and subsequent convolution with the response of a Wood-Anderson instrument. We only calculated magnitudes for earthquakes with a

signal-to-noise ratio higher than 1.5. The final code is available as a supplement to this paper at https://github.com/ricky-gg/LocMagInv.

We tested the code using the identical procedure on all the waveforms available for the cataloged events between November 1, 2018-November 30, 2018 in Southern California, where comparison to the tabulation and relationships given by Richter (1945) and Kanamori et al. (1993) are possible and the waveform data was provided by the Southern California Earthquake Data Center (SCEDC). This 1-month period has a comparable number of earthquakes to the Okmok dataset. As shown, in Figure 3, the comparison is excellent with the resulting inverted attenuation relationship matching well the previously determined attenuation function.

Utilizing the same procedure at Okmok, we find a much stronger attenuation, which is expected on an active volcanic region (Figure 3). This attenuation relationship corresponds to values of α and K of -0.865 and -0.02021, respectively, with hypocentral distance R measured in kilometers. The strong local attenuation is the reason that the magnitude relationship needed to be solved locally. We then proceed to utilize this newly developed magnitude scale for the rest of this study.

Observations

Timing of Earthquakes

Figure 4 plots the primary features of the temporal evolution of the eruption inside the caldera in order to diagnose any possible relationship between the failure of the rocks in the edifice and other physical processes. First, the main bursts of seismicity

are not concurrent with the clusters of observed plumes. Whether the bursts of earthquakes precede or follow the extrusion of ash or steam columns cannot be resolved given the resolution of the plume heights data set. However, it is clear that the seismicity does not increase coincident with the eruptive episodes as might be expected if the primary forcing on the solid rock was the opening of the conduit or the erosive power of the eruption. Instead, after the initial burst on July 12, the seismicity is strongest on July 27, July 30 and Aug. 20, which immediately follow the plume forming events. The last data is a particularly significant increase in the number of small events immediately after the last observed plumes, which marked the official end of the eruption.

The lack of detected earthquakes during plume-forming stages might be thought to be a result of high noise level or lack of telemetered data during the most violent parts of the eruption. Indeed, data outages and noise levels are factors; however, we show in Supplemental Figures S1 and S2, that neither of them correspond to the seismicity pattern in Figure 4. The only obvious effect of the outages is the opposite. Immediately after the initial plume on July 12, a data outage precludes detection of any post-plume seismicity. The cross-correlation between the percent of stations available in each hour and the detected earthquake rate is 0.04 (R^2=0.0016), which corresponds to a p-value of 0.19. (Typically a p-value below 0.05 is required as evidence for statistical significance.) Moreover, the observed correlation is positive, not negative as would be expected for increased outages resulting in low observed seismicity. Therefore, there is no statistical evidence of an anti-correlation between outages and seismicity rate. We

also evaluate the effect of noise by imposing a magnitude threshold level on the catalog. In Figure 4, we limit the entire catalog to magnitudes that are detectable during the high noise, co-eruptive period. This limiting magnitude of completeness is 1.2 and we still observe an increase of seismicity following the timing of the observed plumes. Therefore, we interpret the anti-correlation between plume formation and seismicity rate as a physical phenomenon.

Figure 4 also shows the difference of performance between the different methods used to find earthquakes above the imposed completeness of M_L 1.2. FAST utilizing at least 3 stations detected 1726 events whereas template matching alone on 3 stations detected 612 (Note: Figure 2 includes one-station detections for the template matching results which total 2883; Since FAST is not as strict in event identification, it is not used until there are at least 3 stations detecting the event). Overall, when we include the one-station template matched detections, the FAST detections, and the original catalog from AVO, we have 3926 earthquakes each of which is distinct with an arrival time more than 10 s from any other event. However, only 3557 of those 3926 earthquakes had a signal-to-noise ratio higher or equal to the imposed threshold (1.5) to be assigned a magnitude. This number of events is about an order of magnitude increase from the 419 earthquakes in the original catalog. Interestingly, FAST, the unsupervised method, is far superior to template matching starting at the end of the eruption, where the earthquakes are smaller and seem to come from a source in the south-west region of the caldera as it is shown in more detail in Figure S8 of Section 4 of the Supplementary Materials. Conversely, template matching, the supervised method, seems to perform better during

the eruption, especially during the times of the most prominent bursts, where the number of available templates to search the continuous data was greater. Further details on the comparison of the methods is shown in the supplement Section 5 (Figures S10, S11 and S12).

Location of Earthquakes

The locations in the original earthquake catalog provided by AVO (Figure S6 upper panel) are too scattered to be able to see any structures. However, after applying the double-difference/clustering algorithm, we can clearly see that the seismicity follows a circular pattern around the edges of the caldera (Figure S6). We interpret the relocated earthquakes as highlighting the nested ring fault structure suggested by Byers (1959) to have formed during the caldera-forming collapses of the volcanic edifice. Lu et al. (2010) previously proposed the ring fault as the pathway of the magma to the surface (Lu et al., 2010). The locations are consistent with those found by Ohlendorf et al. (2014), but the relocations provided by Growclust allow the ring structure to be seen for the first time.

We can see that most of the intra-caldera co-eruptive seismicity occurred in the region where the eruption developed and in the vicinity of the peripherally distributed cones. Even though none of these cones showed magmatic activity during the 2008 eruption, it would seem as if they were all still related to the main shallow magmatic reservoir. One possibility is that the pressurization of the reservoir induces an elastic

effect in the whole caldera system by stressing the rocks around it, or alternatively it triggers earthquakes along the ring-fault by injecting fluids into it.

Figure 6 shows the location of the earthquakes of the most prominent increases in seismicity rate throughout the eruption. The first surge of earthquakes appear directly underneath the area where the maar-like craters, the collapse pits and the new tephra cone Ahmanilix emerged. This is the vent opening stage of the eruption, where it is possible that the pressurization of fluids in that area caused the brittle failure of rocks and consequently creating the new vents. The major bursts corresponding to the vent widening phase, are located at the Ahmanilix tephra cone and east of Cone E, respectively. While the former concurs in time with field observations of the drainage at North Cone D Lake, the location of the latter is somewhat surprising and remains a conundrum. It is after this second vent-widening phase large burst at Cone E that seismicity rate, number of observed plumes and plume heights start decreasing leading up to the arrest of the eruption. The last prominent burst consists of smaller and deeper earthquakes that emerge at the ending of the eruption, most of them at the south-west of the caldera. Average depth increases at the end of the eruption as shown in Figure S7, although this may be a detectability issue as discussed below. The cumulative seismicity (Figure S9) and supplementary movie provides another window into the aggregate behavior. The main features that are highlighted by the triggered earthquakes during the eruption are the ring-fault structure of the caldera, a long >15km lineation striking SW-NE starting at the edge of the caldera near Cone A and ending close to Inanudak Bay in the south-west sector of the volcano, a ~10km long NW-SE

striking cluster off-shore to the south-east of the volcano, and a group of clusters in the geothermal area surrounding Steeple Point, also in the south-east of Okmok volcano.

Discussion

Clog and Crack

What does the detailed seismicity tell us about the eruptive sequence? The key observations are that the eruption is bracketed by large bursts of seismicity with a secondary burst on days around July 27, the bursts are not correlated with the plumes and that the seismicity collocates with the caldera rim and cones, including cones not otherwise active in this eruption. All of these observations point to a transient forcing associated with pressurization during the closed phases of the eruption. We suggest that when a parcel of over-pressurized, hot magma or other fluid is trapped in a closed system, the clogging pressurizes the surrounding rock, which eventually cracks. We therefore call this pattern clog and crack. Once the pathways have been created this parcel of fluids will experience an instantaneous depressurization and expansion, causing an explosion which is followed by a plume of hot gases and lithics. However, it seems like the pressure accumulated by a single parcel is not enough to maintain the open system, so the conduits being used for material ejection collapse, closing the system and re-starting the cycle.

The clog and crack framework explains the fact that the bursts of earthquakes are not synchronous with the observed plumes. The greatest forcing on the solid rock is during

the clogged (closed) phases. Under significant confining pressure or an increase in normal stress, rocks experience shear failure (Jaeger et al., 2007), which is observed as earthquakes. Open eruptive phases allow relatively easy depressurization and therefore do not result in significant compression or failure. One could imagine that conduit pressure during the eruption or collapse could have dominated the seismicity, but this does not appear to be the case. Conduit closure at the end of each extrusive episode appears to happen aseismically, perhaps due to closure by rubble or other materials. It is not a catastrophic failure as envisioned by Kennedy et al. (2005) for a Vulcanian eruption. The 2008 Okmok eruption also lacks a prolonged effusive stage, similar to the 1997 eruption, that would be indicative of a sustained open phase. Instead, the system is only transiently and sporadically open.

Similar variations in seismicity were documented by Shiro et al. (2018) and Shelly and Thelen (2019) during the 2018 caldera collapse eruption at Kilauea volcano. There, the seismicity rate changed cyclically from high rates to periods of relative quiescence post-collapse. Okmok did not exhibit such cyclic behavior and is more challenging to track due to the ongoing explosive eruption, but it, too, seems to have lower seismicity when the vent is open. The 2008 Okmok eruption is also different from the 2018 Kilauea summit eruption in that it is driven by an intrusion of magma rather than an evacuation of the chamber to the flank. Nonetheless, the combination of observations raises the intriguing possibility that seismicity restricted to the closed stages of an eruption is a general behavior.

The localization of the seismicity near the ring fault is also consistent with the clog and crack concept. The earthquakes are clustering around the fluid pathways as also suggested by Ohlendorf et al. (2014), which suggests that their cause is in fact the pressurization of the fluid during its ascent. Perhaps earthquakes rate is a proxy for intrusion rate while extrusion rate is more directly caught by other parameters, such as eruptive tremor.

A further test of the role of pressurization could potentially be the sense of motion on faults from focal mechanisms. Unfortunately, the small number of stations at Okmok combined with the small magnitude events prevent us from calculating focal mechanisms. Ohlendorf et al. (2014) already demonstrated that the data permits a diversity of stress states.

The clog-and-crack cycle repeats itself as the shallow reservoir emits pulses of fluids until enough material has been ejected and the system-wide pressure has reduced so much that it cannot overcome the lithostatic pressure, and the eruption effectively ceases. At the end of the eruption, as noted by Lu and Dzurisin (2010), once the volcano becomes a closed system once again, the pressure gradient between the shallow reservoir and the deeper sources of magma starts driving fluids into the former, instantaneously commencing a stage of shallow reservoir replenishment. This final process is very well captured by the seismic network and most of the events lay in a south-west trending lineation which starts at the edge of the caldera and extends almost to Inanudak Bay.

Further evidence for fluid-seismic coupling

The rich catalog of the Okmok eruptive earthquakes contains more detailed evidence for hydrological interactions at a finer scale. The bulk of this evidence comes from putting the earthquakes in their geological and hydrological context.

The caldera floor at Okmok has a topographic slope towards the northeast (Lu and Dzurisin (2), 2008) which seems to have a major control on the hydrological system. In fact, the outflow from the caldera is through a steeply carved gorge in the northeast sector called Crater Creek gorge and its entrance to the caldera is referred to as The Gates (Fig. 1 inset). Furthermore, active fumaroles and thermal springs have been reported at Cone C and Cone D, respectively, for as long as 50 years before the eruption (Byers, 1959, Larsen et al., 2015) and are still active as of 2020. Even though Cone A (south) is constantly steaming, it lacks obvious signs of hydrothermal alteration like that observed at the summit of Cone C. Additionally, Cone E (southwest) has a long-lived crater lake that does not seem to be continuously altered by hydrothermal activity but that was observed to have signs of roiling shortly after the 2008 eruption (Larsen et al., 2015).

Based on the seismic quiescence preceding the eruption, combined with the observation of a subtle increase in the inflation rate and the migration of the deformation source before the onset (Feymueller and Kaufman, 2010; Lu et al., 2010; Albright et al., 2019) and the vigorous burst of earthquakes just a few hours before the beginning which are localized beneath the area of the eruption, the data suggests an aseismic migration of magma from the top of the shallow storage zone, estimated to be located at

3.5 km depth and at the center of the caldera (Lu and Dzurisin, 2010; Albright et al., 2019), towards the north sector of the caldera through a series of dikes and sills. The first burst of earthquakes of the eruption have magnitudes that increase towards the end of the burst and the beginning of the exhalation of magmatic and steam plumes (Figure 5a). As the hydrological system of the caldera started feeling the effect of the heat of the propagating magma, the host rocks may have experienced a large increase in pore-pressure leading to an effective triggering of cracks. The now high-permeability damaged zone where the cracks developed could have served as the preferential pathway of the magma, creating a positive-feedback between magma migration and fluid pressurization up to the point where the lithostatic pressure was exceeded and the first phreatomagmatic explosion occurred. The seismicity following or accompanying the vent opening stage most likely reflects the breaking of the rocks underneath and around the vents as well as the emergence of the collapse pits described by Larsen et al. (2015).

Interestingly, the eruption not only triggered earthquakes where it developed, but it also created disturbances in the hydrological systems of the various intra-caldera cones. The earthquakes that cluster around Cone E throughout the eruption are a sign of pressurization in that area of the caldera ring-fault (See Supplemental Animation). Besides the migration of most fluids in the reservoir to the north, it is possible that fluids also found their way through cracks and fractured areas in all directions toward the ring-fault. Thus, the temporary roiling observed at Cone E by AVO personnel right after the eruption ended could be a surface expression of these potentially hot fluids (Larsen

et al., 2015).

The end of the eruption shows a great increase in the number of detected small earthquakes. Even though the reduction in completeness after the end of the eruption could be related to a lower noise level, it is clear that there are many smaller and deeper earthquakes that delineate a feature that extends ~15 km from the SW edge of Okmok Caldera to Inanudak Bay. This large structure could be the plumbing system that Okmok uses as a lateral drainage during caldera forming events such as the ones observed at Kilauea, Bardarbunga and Miyake-jima volcanoes. This large burst of small earthquakes was not accompanied by any observation of fluids coming out, Okmok apparently remained clogged.

Conclusions

We increased the number of observed earthquakes during the 2008 Okmok eruption by almost one order of magnitude by utilizing template matching and supplementing the work with FAST detections and refined locations. Assessing completeness required consistently assigned magnitudes based on a simultaneously inverted attenuation relationship for Okmok. This magnitude assigned with the attenuation inversion process is codified in a new, publically released code.

The time series of earthquake rate in the enhanced catalog shows that seismicity can track the dynamic evolution of the eruption with greater detail than any other geophysical methods at Okmok. We have found that the long-lived eruption developed in cycles where the system was rapidly alternating from open to closed. We call this a

clog and crack scenario. The initial seismic sequence highlights the vent opening phase of the eruption where pressurization was the highest. The magma intrusion triggered a prominent burst of earthquakes which created new pathways for magmatic and other fluids to the surface. Once the magmatic fluids and accompanying steam were ejected, seismicity decreased dramatically, until the plumes started losing height and the system became clogged again, allowing for a new cycle of pressure build up which is observed by an increase of number of earthquakes in distinct areas of the caldera. The sequence repeats itself at varying intensities until the overall pressure is no longer high enough to erupt, and then ends with one last, deep, final burst of seismicity.

Figures

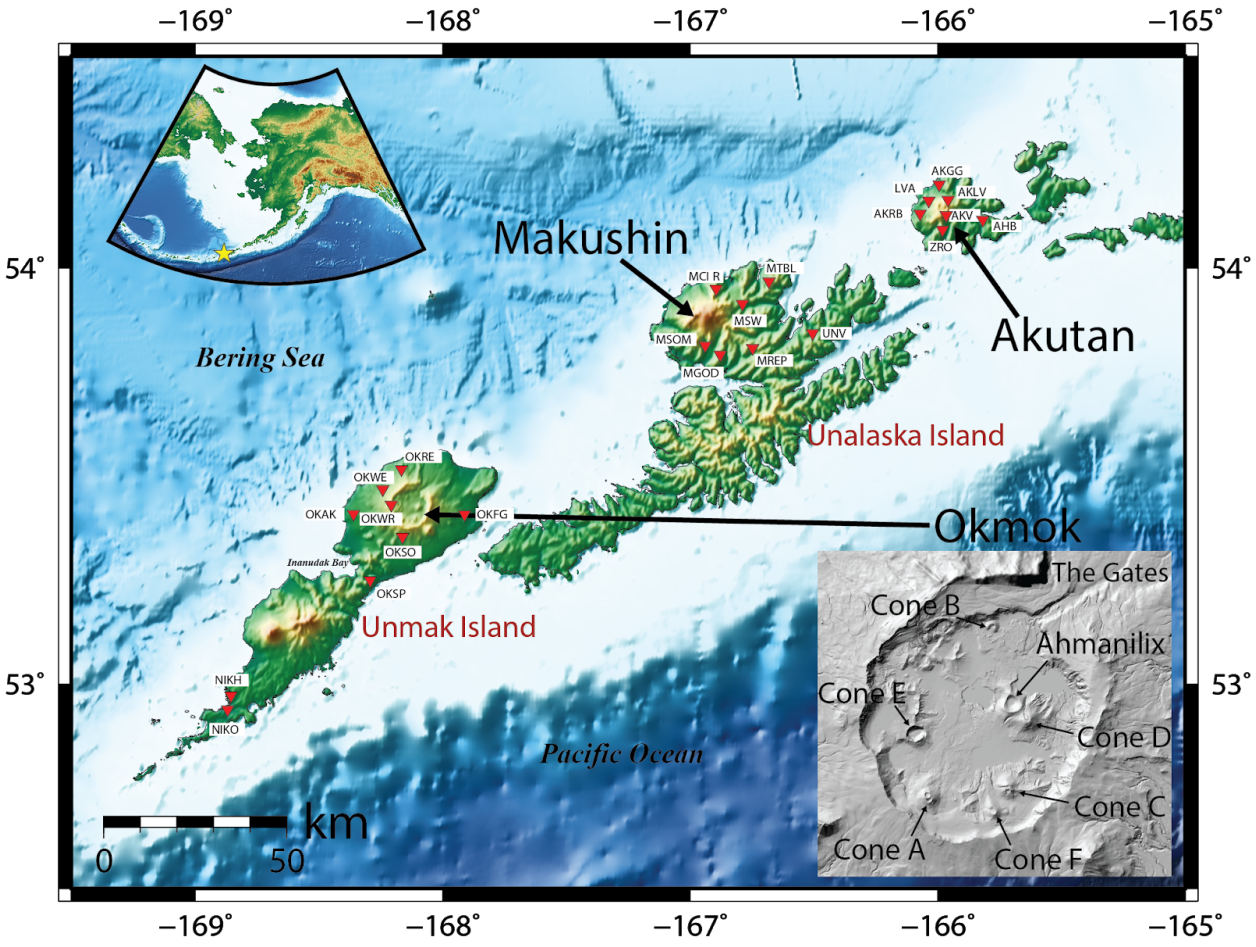

Figure 1. Map of the seismic stations (triangles) used for this study with an inset showing the location of the intra-caldera cones.

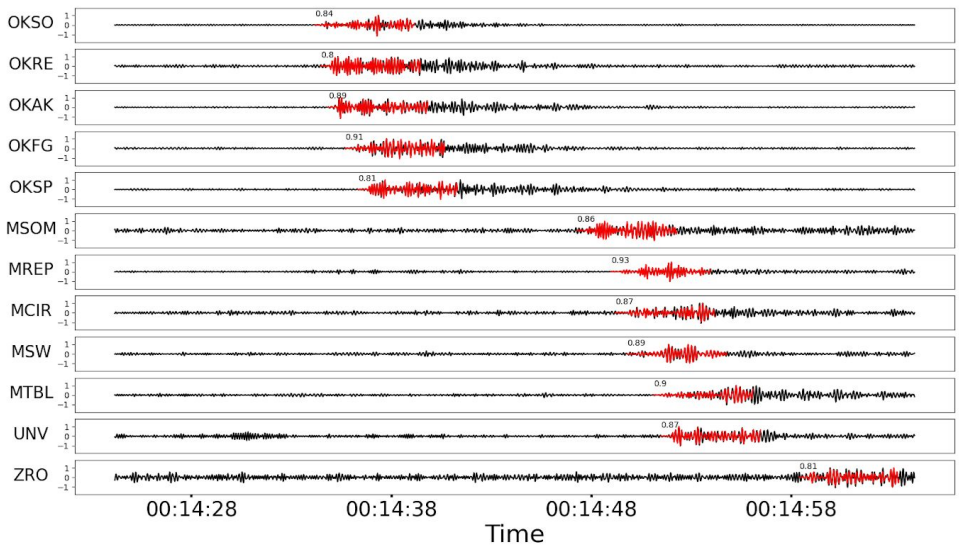

Figure 2. Example of detections using template matching. Red is the template and black is continuous data. This example has mean cross-correlation of 0.87, individual cross-correlations are shown on top of each trace. (See also Figures S3, S4 and S5 for further examples).

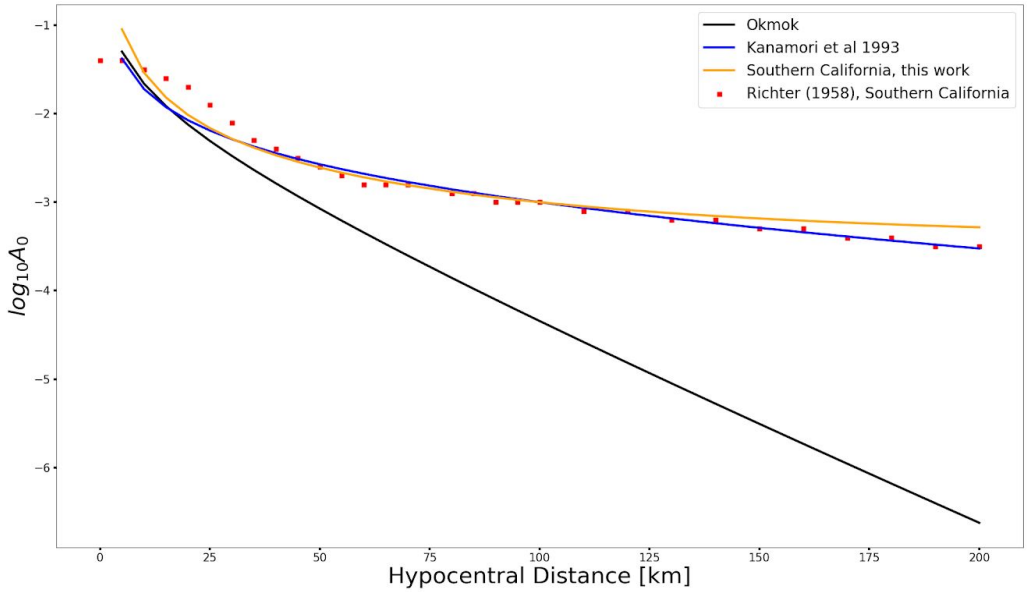

Figure 3. Attenuation relationship (Equation 2) for the 2008 Okmok eruption (black) as derived by simultaneous inversion of magnitudes and attenuation as described in the text. The red squares represent the tabulation made by Richter (1958) and the blue line represents the relationship computed by Kanamori et al. (1993) to calibrate M_L in Southern California. The method successfully reproduces the known attenuation relationship for Southern California and shows that the attenuation in this particular region of active volcanoes in the Aleutians is much stronger.

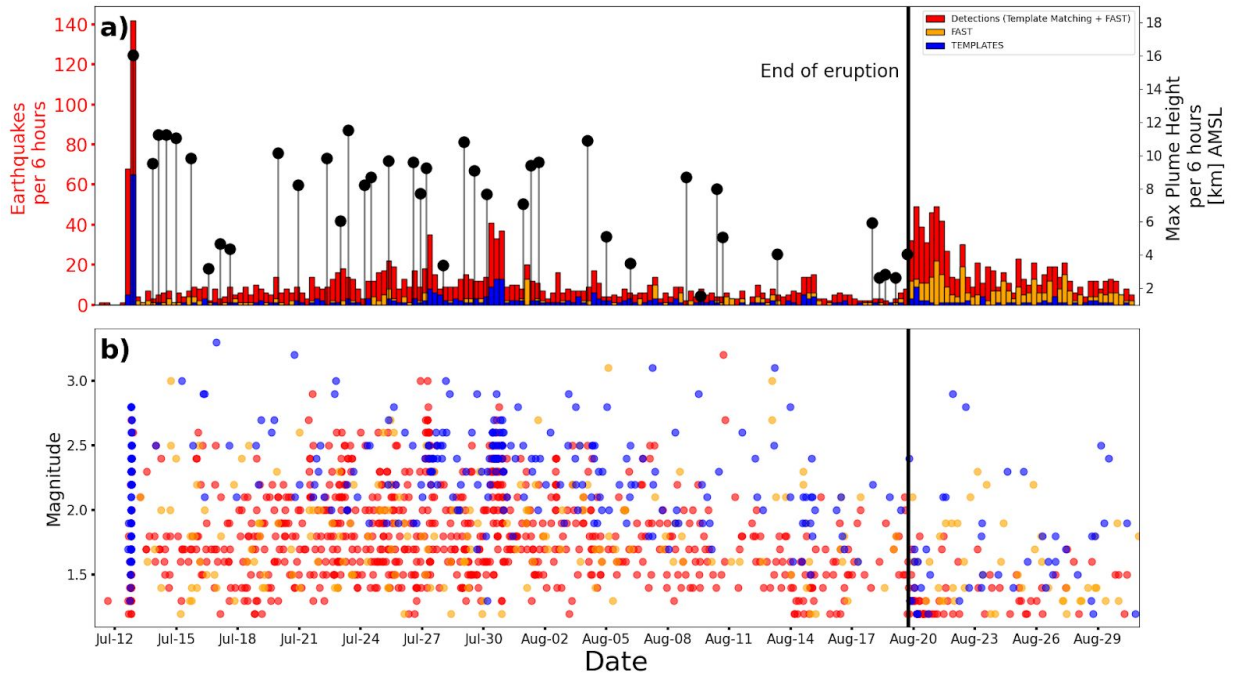

Figure 4. a) Time series of the earthquake rate (bars) as shown by the original AVO catalog (blue), the events detected using the FAST method that were not found by the template matching technique (orange) and the final new catalog including templates, template matched events and FAST events (red) compared to the maximum plume heights observed in periods of 12 hours (stem). Only earthquakes with magnitudes equal to or above M_L1.2 are shown. b) Temporal distribution of the re-calculated magnitudes for the AVO catalog (blue), the new FAST events (orange) and the template matched events (red).

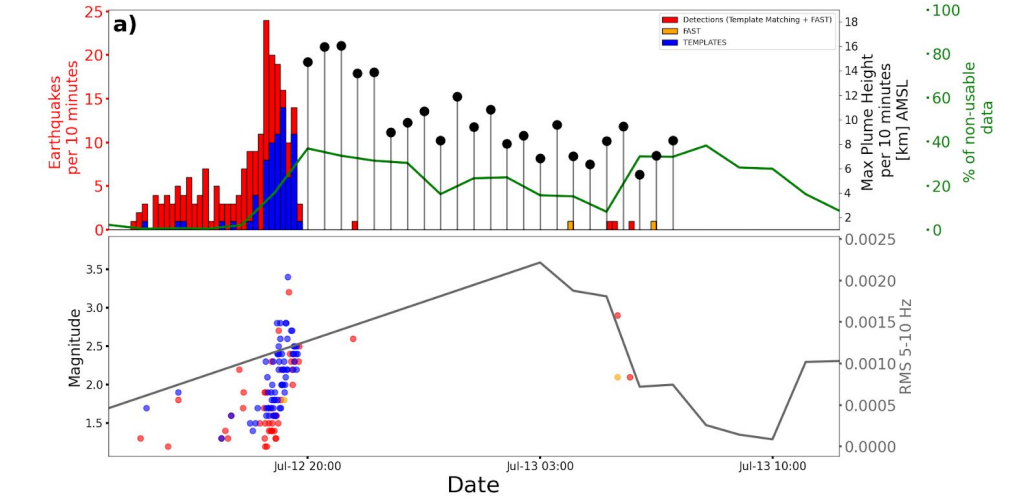
a)
Detections (Template Matching + FAST)
FAST
TEMPLATES
Earthquakes per 10 minutes
Max Plume Height per 10 minutes [km] AMSL
% of non-usable data
Magnitude
RMS 5-10 Hz
Jul-12 20:00
Jul-13 03:00
Jul-13 10:00
Date

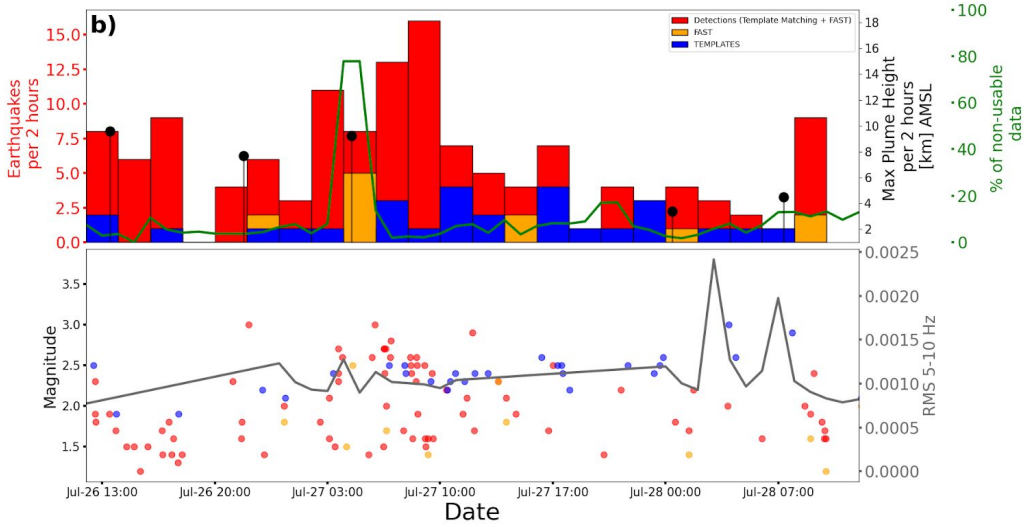
b)
Detections (Template Matching + FAST)
FAST
TEMPLATES
Earthquakes per 2 hours
Max Plume Height per 2 hours [km] AMSL
% of non-usable data
Magnitude
RMS 5-10 Hz
Jul-26 13:00
Jul-26 20:00
Jul-27 03:00
Jul-27 10:00
Jul-27 17:00
Jul-28 00:00
Jul-28 07:00
Date

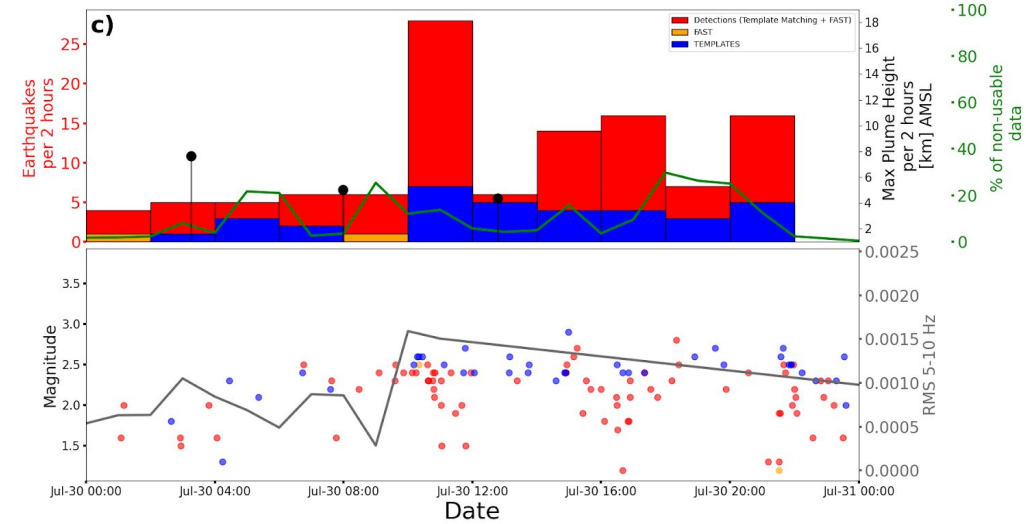
c)
Detections (Template Matching + FAST)
FAST
TEMPLATES
Earthquakes per 2 hours
Max Plume Height per 2 hours [km] AMSL
% of non-usable data
Magnitude
RMS 5-10 Hz
Jul-30 00:00
Jul-30 04:00
Jul-30 08:00
Jul-30 12:00
Jul-30 16:00
Jul-30 20:00
Jul-31 00:00
Date

Fig. 5 Earthquake rate and maximum plume heights for 3 different periods of earthquakes bursts in the eruption: a) The run-up sequence of the eruption, note the increase in size of earthquakes as it approaches the onset of the eruption. This lack of detection during the initial eruptive plume is possibly due to data quality. This is to be contrasted with other plume episodes where the lack of detections is not well-explained by noise. ; b) Large surge of earthquakes in the middle of the eruptive sequence, this period correlates in time with field and satellite observations of the drainage of North Cone D Lake; c) The largest surge of earthquakes in the middle of the eruption after which earthquake rate and plumes numbers and heights start decreasing until the end of the eruption. The green line in the top panel represents the percentage of non-available data for 1 hour bins. The gray line in the bottom panel represents the average RMS amplitude of the waveforms filtered between 5 and 10 Hz and normalized by the dynamic range for all stations. As in figure 4, only earthquakes with a magnitude equal to or above M_L1.2 are shown.

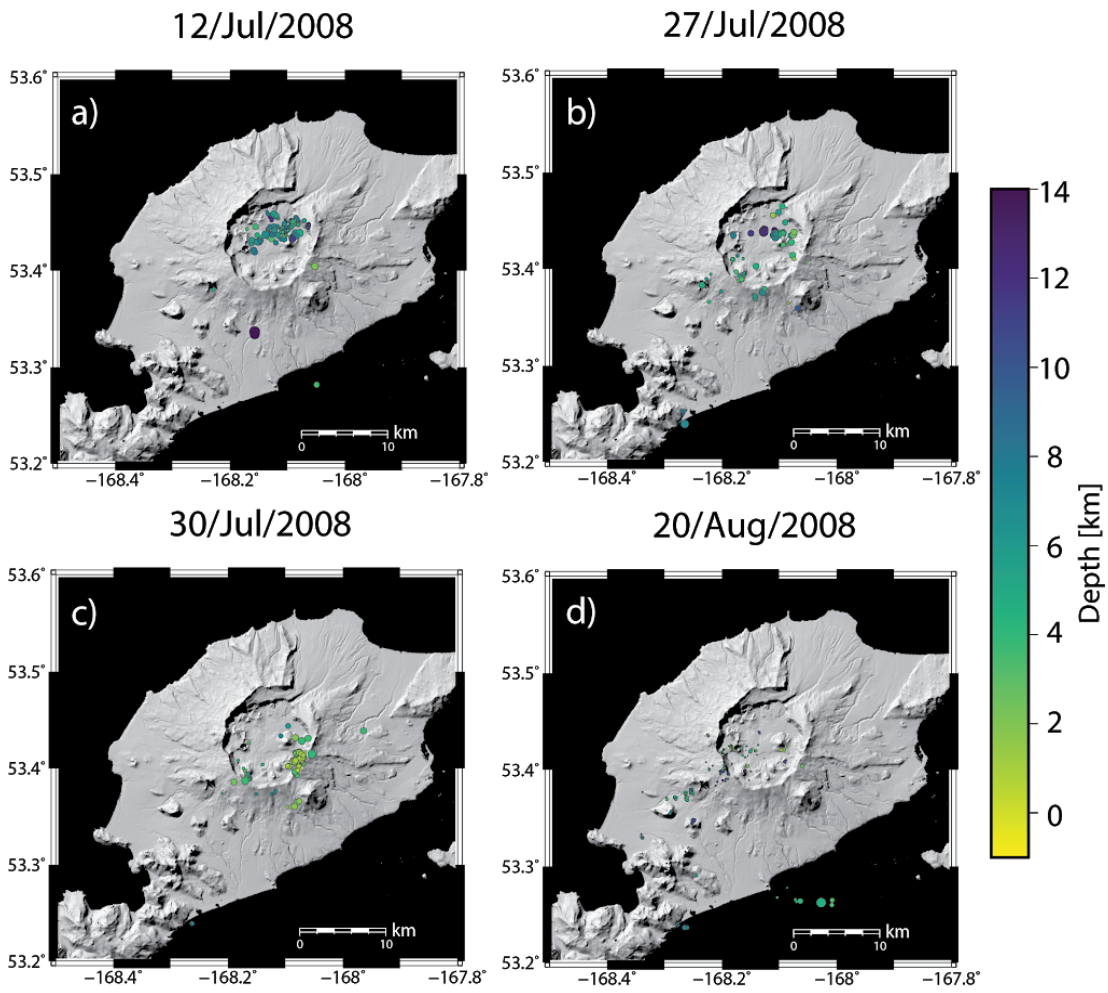

Figure 6. Seismicity maps at the times of the most prominent bursts of earthquakes during the eruption. a) July 12, the vent opening sequence. b) July 27, second largest burst of earthquakes in the vent widening phase (top panel in Figure 5), most of the earthquakes during this day occurred directly below the North Cone D Lake vent and are likely associated to the drainage of the lake into the vent as described in more detail in the text. c) July 30, largest seismic burst in the vent widening phase of the eruption (bottom panel in Figure 5), the events cluster East-North-East of cone C, ~3 km away from the closest active eruptive vent. d) August 20, one

day after the eruption ceased, there is a large burst of smaller/deeper earthquakes that maps a NE-SW striking structure.

References

Albright, J. A., Gregg, P. M., Lu, Z., & Freymueller, J. T. (2019). Hindcasting magma reservoir stability preceding the 2008 eruption of Okmok, Alaska. Geophysical Research Letters, 46(15), 8801-8808.

Bebbington, M. S. (2007). Identifying volcanic regimes using hidden Markov models. Geophysical Journal International, 171(2), 921-942.

Bebbington, M. S. (2014). Long-term forecasting of volcanic explosivity. Geophysical Journal International, 197(3), 1500-1515.

Beyreuther, M., Barsch, R., Krischer, L., Megies, T., Behr, Y., & Wassermann, J. (2010). ObsPy: A Python toolbox for seismology. Seismological Research Letters, 81(3), 530-533.

Byers Jr, F. M., & Brannock, W. W. (1949). Volcanic activity on Umnak and Great Sitkin Islands, 1946–1948. Eos, Transactions American Geophysical Union, 30(5), 719-734.

Byers, F. M. (1959). Geology of Umnak and Bogoslof Islands, Aleutian Islands, Alaska.

Chamberlain, C. J., Hopp, C. J., Boese, C. M., Warren-Smith, E., Chambers, D., Chu, S. X., ... & Townend, J. (2018). EQcorrscan: Repeating and Near-Repeating Earthquake Detection and Analysis in Python. Seismological Research Letters, 89(1), 173-181.

Dixon, J. P., & Stihler, S. D. (2009). Catalog of earthquake hypocenters at Alaskan volcanoes: January 1 through December 31, 2008. US Geol Surv Data Ser, 467, 86.

Freymueller, J. T., & Kaufman, A. M. (2010). Changes in the magma system during the 2008 eruption of Okmok volcano, Alaska, based on GPS measurements. Journal of Geophysical Research: Solid Earth, 115(B12).

Grey, D. M. (2003). Post-caldera eruptions at Okmok volcano, Umnak Island, Alaska, with emphasis on recent eruptions from Cone A (Doctoral dissertation).

Haney, M. M. (2010), Location and mechanism of very long period tremor during the 2008 eruption of Okmok Volcano from interstation arrival times, *J. Geophys. Res.*, 115, B00B05, doi:10.1029/2010JB007440.

Haney, M. M. (2014), Backprojection of volcanic tremor, *Geophys. Res. Lett.*, 41, 1923– 1928, doi:10.1002/2013GL058836.

Jaeger, J. C., Cook, N. G., & Zimmerman, R. (2007). Fundamentals of Rock Mechanics (4th ed.). Malden, MA: Blackwell Publishing Ltd.

Johnson, J. H., Prejean, S., Savage, M. K., & Townend, J. (2010). Anisotropy, repeating earthquakes, and seismicity associated with the 2008 eruption of Okmok volcano, Alaska. Journal of Geophysical Research: Solid Earth, 115(B9).

Kennedy, B., Spieler, O., Scheu, B., Kueppers, U., Taddeucci, J., & Dingwell, D. B. (2005). Conduit implosion during Vulcanian eruptions. *Geology*, *33*(7), 581–584. https://doi.org/10.1130/G21488.1

Lahr, J. C. (1999). HYPOELLIPSE: A computer program for determining local earthquake hypocentral parameters, magnitude, and first motion pattern (p. 119). Denver, Colorado: US Geological Survey.

Larsen, J. F., Schaefer, C. A., Kaufman, J. R., & AM Lu, Z. (2015). The 2008 phreatomagmatic eruption of Okmok Volcano, Aleutian Islands, Alaska: Chronology, deposits, and landform changes.

Larsen, J. F., Śliwiński, M. G., Nye, C., Cameron, C., & Schaefer, J. R. (2013). The 2008 eruption of Okmok Volcano, Alaska: Petrological and geochemical constraints on the subsurface magma plumbing system. Journal of Volcanology and Geothermal Research, 264, 85-106.

Larsen, J., Neal, C., Webley, P., Freymueller, J., Haney, M., McNutt, S., Schneider, D., Prejean, S., Schaefer, J. and Wessels, R. (2009). Eruption of Alaska volcano breaks historic pattern. Eos, Transactions American Geophysical Union, 90(20), 173-174.

Lu, Z., & Dzurisin, D. (2010). Ground surface deformation patterns, magma supply, and magma storage at Okmok volcano, Alaska, from InSAR analysis: 2. Coeruptive deflation, July–August 2008. Journal of Geophysical Research: Solid Earth, 115(B5).

Lu, Z., Dzurisin, D., Biggs, J., Wicks Jr, C., & McNutt, S. (2010). Ground surface deformation patterns, magma supply, and magma storage at Okmok volcano, Alaska, from InSAR analysis: 1. Intereruption deformation, 1997–2008. Journal of Geophysical Research: Solid Earth, 115(B5).

Menke, W. (2018). *Geophysical data analysis: Discrete inverse theory*. Academic press.

National Academies of Sciences, Engineering, and Medicine. (2017). Volcanic eruptions and their repose, unrest, precursors, and timing. National Academies Press.

Ohlendorf, S. J., Thurber, C. H., Pesicek, J. D. & Prejean, S. G. Seismicity and seismic structure at Okmok Volcano, Alaska. *Journal of Volcanology and Geothermal Research* **278–279**, 103–119 (2014).

Ross, Z. E., Trugman, D. T., Hauksson, E., & Shearer, P. M. (2019). Searching for hidden earthquakes in Southern California. Science, 364(6442), 767-771.

Shelly, D. R., Beroza, G. C., & Ide, S. (2007). Non-volcanic tremor and low-frequency earthquake swarms. *Nature*, *446*(7133), 305-307.

Shelly, D. R., & Thelen, W. A. (2019). Anatomy of a Caldera Collapse: Kīlauea 2018 Summit Seismicity Sequence in High Resolution. *Geophysical Research Letters*.

Shiro, B., Burgess, M. K., Chang, J. C., Dotray, P., Okubo, P., Thelen, W. A., ... & Montgomery-Brown, E. K. (2018, December). Earthquake sequences of the 2018 Kilauea Volcano eruption. In *AGU Fall Meeting Abstracts*.

Sparks, R. S. J. (2003). Forecasting volcanic eruptions. Earth and Planetary Science Letters, 210(1-2), 1-15.

Trugman, D. T., & Shearer, P. M. (2017). GrowClust: A hierarchical clustering algorithm for relative earthquake relocation, with application to the Spanish Springs and Sheldon, Nevada, earthquake sequences. Seismological Research Letters, 88(2A), 379-391.

Wech, A., Tepp, G., Lyons, J., & Haney, M. (2018). Using earthquakes, T waves, and infrasound to investigate the eruption of Bogoslof volcano, Alaska. *Geophysical Research Letters*, *45*(14), 6918-6925.

Yoon, C. E., O'Reilly, O., Bergen, K. J., & Beroza, G. C. (2015). Earthquake detection through computationally efficient similarity search. *Science advances*, *1*(11), e1501057.

Acknowledgements

We are grateful to the staff of the Alaska Volcano Observatory for their heroic work in collecting the key data of this paper and their insightful feedback throughout this project. P. Webley generously provided the plume height data. This work was conducted with the This work was supported in part by a Mexican National Council forScience and Technology (CONACYT) Doctoral Scholarship to Garza-Giron and in part by NSF EAR-1761987. We are grateful to The Generic Mapping Tools (GMT) for the mapping tools, and The Alaska Division of Geological and Geophysical Surveys (ADGGS) for the DEM.

Data and Materials

The waveform data was provided by staff of the Alaska Volcano Observatory and is now available via IRIS DMC. The template matching was done using EQCorrScan

(https://github.com/eqcorrscan/EQcorrscan) and FAST detections using the code available at (https://github.com/stanford-futuredata/FAST). The final catalogs from this work are available at https://github.com/ricky-gg/Okmok_2008 and the code LocMagInv utilized for magnitude determination is at https://github.com/ricky-gg/LocMagInv